International Journal of Mechanical Sciences 146–147 (2018) 295–302

Contents lists available at ScienceDirect

International Journal of Mechanical Sciences

journal homepage: www.elsevier.com/locate/ijmecsci

Shear stress triggering brittle shear fracturing of rock-like materials

Lifeng Ma [a], Nina Yari [b,*], Marian Wiercigroch [b]

[a] S&V Lab, Department of Engineering Mechanics, Xi'an Jiaotong University, Xi'an 710049 China
[b] Centre for Applied Dynamics Research, School of Engineering, University of Aberdeen, Aberdeen AB24 3UE, UK

ARTICLE INFO

Keywords:
Brittle shear fracturing
Rock-like materials
Contact mechanics
Conical crack
J-integral

ABSTRACT

Contact fracturing of rock-like brittle materials indented by rigid cylindrical punches with flat ends is studied. Contrary to the classical shear fracturing mechanism of brittle materials explained in terms of multi-tensile-stressed micro-cracks in materials [1], a new mechanism dominant in brittle shear fracturing is found, namely, shear stress triggered fracturing orientation existing in nature, and the contact crack initiation angle for such kind rock-like materials is also revealed. This phenomenon is very different from such as Hertzian or Roesler's [2] crack generation mechanism, as cracks are directed inwards rather than outwards. The theoretical predictions are validated by our experimental results. This finding testifies that for a rock-like brittle material shear fracturing along its maximum shear stress plane is possible under some special confinement, which has important implications for seismology and rock-mass stability, as well as rock engineering.

1. Introduction

Hertz first investigated contact fracturing between glass lenses in the 1880s. Since then, great efforts have been devoted to such kind of brittle fracturing problem. It has been confirmed that, the Hertzian contact cracks always initiate from contacted surface and then advance into the contacted body with an outward conical profile (e.g. see [3]). This Hertzian contact fracturing looks simple but it is really a challenging one, in literature, which has been studied by numerous researchers. The detailed experimental and theoretical progresses on this problem as well as its development history have been reported and intensively reviewed, (see, e.g. [3–8]). However, the Hertzian conical crack problem is still open despite the fact that it has been studied over 100 years and there are two main reasons for this. The first one is associated with the contact damage approach which can be used as a simple and practical technique for evaluating some strength-related properties of materials such as fracture toughness and surface hardness. The second reason, also an intriguing one, relates to the fact that until to now, it has been difficult to achieve a satisfactory quantitative explanation to describe the initiation and growth of this type of crack in terms of the conventional fracture mechanics. There are two major unresolved issues remaining, namely, (i) the geometrical location of the initiated conical crack, and (ii) contact crack initiation and propagation model, which may directly reflects the material mechanical properties.

The classical Hertzian contact tests using a spherical indenter look simple but in fact they are complex as the contact area increases for larger indentation loads, and therefore the surface trace of an initiated conical crack can be easily engulfed by the expanding contact circle, which causes secondary fracture because of the indentation load acting over the cone crack and the supporting material underneath [9]. Also, stress trajectories move as the radius of contact increases, making any analytical attempt untraceable. In comparison with the Hertzian contact, the well-known tests conducted by Roesler [2] using a flat and square-ended cylindrical indenter generates a complete contact that may be simpler to study (see Fig. 1). This is because its contacting area is unchanged and both displacement and traction conditions at the contacting surface are given in a simple form, greatly reducing the difficulty of stress analysis. It has been found that the feature of contact stress field in substrate is similar to one of the circumferentially cracked cylindrical rod specimen [10]. The stress singularity at the contact edge plays a significant role in the conical crack formation and its initiation angle.

On the other hand, the brittle fracturing of rocks has been widely and intensively studied in the literature and is still the subject of constant studies (see, e.g. [1,11–20]). With the existing theoretical and experimental results, it has been believed that: (i) when macro-crack in rock material is under tensile load, the crack will straightly advance as any brittle material does; and (ii) when the rock material is under compression, the multi-micro-cracks interaction in them may result tensile stress on micro-cracks, which can trigger micro-cracks growth and coalition, and finally lead 'shear-like, crack growth. In one word, the tensile stress is believed as the fundamental factor for triggering the brittle fracturing of rock materials. By virtue of the flat and square-ended cylindrical indenter, the aim of this paper is to study the contact fracturing of rock-like brittle materials, in order to explore the rock-like materials' properties under this specific condition. The rock-like material here mainly

* Corresponding author.
E-mail addresses: malf@xjtu.edu.cn (L. Ma), nina.yari@abdn.ac.uk (N. Yari), m.wiercigroch@abdn.ac.uk (M. Wiercigroch).

https://doi.org/10.1016/j.ijmecsci.2018.07.008
Received 18 April 2018; Received in revised form 28 June 2018; Accepted 5 July 2018
Available online 27 July 2018

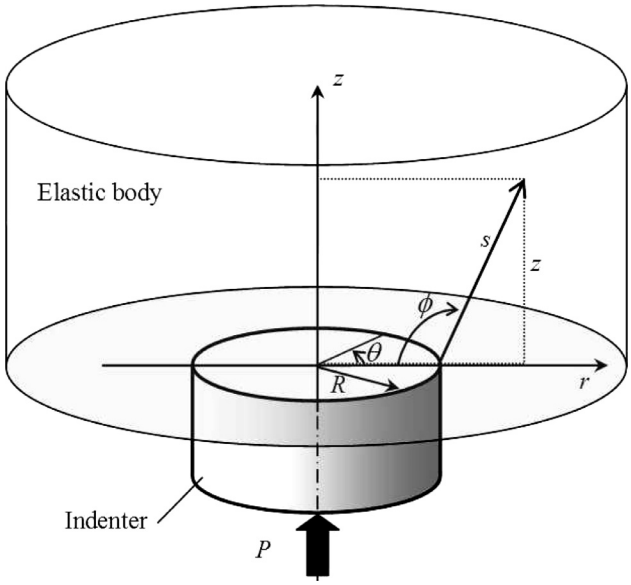

Fig. 1. A schematic showing the upper elastic solid indented by a lower flat-ended rigid punch under normal load P. This coordinate system is convenient for the following elastic deformation analysis.

Nomenclature

A	formed circumferential crack Area
D	diameter of indenter
E	Young's modulus
G	crack initiation energy release rate
h	indentation depth
$J_m(^*)$	the first kind of Bessel function
K_I	indentation depth
l	crack growth length
m_i	surface outward normal unit vector
n_i	crack-tip growth direction
O	origin of coordinates
P	applied normal force
R	contact radius
S	surface of whole half space
S_T	contacted surface
S_u	displacement boundary
T_i	traction acts on the surface
U_{crack}	energy consumed during forming/closing crack
U_{diss}	dissipation energy due to crack surfaces friction
U_E	elastic energy stored in the solid
V	volume of the whole solid
W	external load work
w	strain energy density
x_1, x_2	r-axis and z-axis, respectively
τ_0	friction stress between crack surfaces
ν	Poisson's ratio
σ_{ij}	stress
λ, μ	Lame's elastic constants
ϵ_{ij}	strain
ϕ	contact crack initiation angle

refers to the material like: rock, PMMA, concretes, and the similar. The following related problems will be considered:

(i) *Initiation angle of contact conical cracks.* This problem is still main open problem, although it has been studied by many researchers (see e.g., [21–23]). Roesler's experimental result shows that the angle of contact conical cracks is outwards for *glass material* (see Fig. 2 where the angle is around 22°). Here, to keep the original Roesler's result, we will not convert it to the coordinates depicted in Fig. 1. The question we will be asking: Does this result make sense for rock-like brittle materials?

(ii) *Contact crack initiation and propagation in rock-like materials.* The assumption of contact fracturing criterion, made in almost all relevant prior works, saying that the conical crack should follow the trajectory of the minimum principal stress defined by the preexisting stress field, has been shown invalid by Kocer and Collins [21]. Instead they proposed that the growth of crack is along the direction of maximum strain energy release. On the other hand, Xie et al. [23] employed the maximum energy release rate criterion from classical linear elastic fracture mechanics to predict the contact crack initiation angle. Since their assumptions lack experimental support, their reliability is questionable. New experimental tests are required for further study of this unsolved contact cracking phenomenon, especially for rock-like materials, because of its significance in applications.

(iii) *Shear crack in rock-like materials.* In fracture mechanics, the crack growth and its growth direction is governed by Mode I tensile load, combining or not with Mode II shear load [24]. It is hard to imagine that the crack growth is only controlled by Mode II shear load, because the crack growth under this condition is unstable and the stress state at the crack tip will be shifted to tensile load once it advances. However, this problem inevitably occurring in contact fracturing: *whether shear cracking occurs and can the crack stably propagate in their own plane without turning under such contact condition?* [1,25]. From the mechanics point of view, strictly speaking, there lacks a convincible solution to this tough challenge up to now.

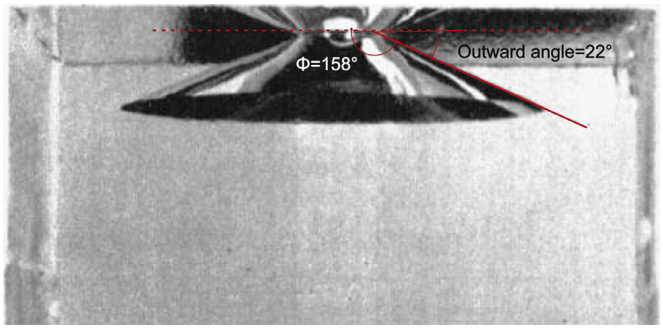

Fig. 2. Roesler's experimental result for a contact conical crack of glass [2]. The angle of outwards conical crack is roughly 22°.

These problems are just different facets of the contact fracturing, and they are rather closely related than separated. Only a full analysis from different aspects of the problem is able to shed some light on the mechanism of the contact fracturing of rock-like materials.

The structure of this paper is as follows: Firstly, the stress field of Roesler's contact model is introduced and modelled in Section 2. Following the analysis, the crack initiation driving force along the contact edge is analyzed in Section 3. With above basic analysis, in Section 4, some plain experimental tests on contact fracturing are conducted and discussed. Finally, some conclusions are drawn in Section 5.

2. Contact stress analysis

In this section the basic contact model is introduced, and the basic stress distribution in the contacted body is provided. We assume, as shown in Fig. 1, the cylindrical indenter with flat end is rigid, the indented elastic solid is large enough to be treated as an infinite solid, compared with the indenter contact size, and the friction effect between contact surfaces will be ignored for simplicity [10].

2.1. Contact stress state

The exact stress state in the half-space has been obtained by Sneddon [26] and it can be expressed as

$$\begin{aligned}
\sigma_{zz} &= -\frac{4\mu(\lambda+\mu)}{(\lambda+2\mu)}\frac{h}{\pi R}(J_1^0+\zeta J_2^0),\\
\sigma_{zr} &= -\frac{4\mu(\lambda+\mu)}{(\lambda+2\mu)}\frac{h}{\pi R}(\zeta J_2^1),\\
\sigma_{\theta\theta} &= -\frac{4\lambda\mu}{\lambda+2\mu}\frac{h}{\pi R}J_1^0-\frac{4\mu^2}{\rho(\lambda+2\mu)}\frac{h}{\pi R}\left(J_0^1-\frac{(\lambda+\mu)}{\mu}\zeta J_2^1\right),\\
\sigma_{rr}+\sigma_{\theta\theta} &= -\frac{4\mu}{(\lambda+2\mu)}\frac{h}{\pi R}\left((2\lambda+\mu)J_1^0-(\lambda+\mu)\zeta J_2^0\right),
\end{aligned} \tag{1}$$

where R is the contact radius, h is the indentation depth that is related to the applied normal force, $P=8\mu(\lambda+\mu)Rh/(\lambda+2\mu)$, λ and μ are Lame's elastic constants, $\rho=r/R$, $\zeta=z/R$, and $J_n^m=\mathrm{Im}[\int_0^\infty t^{n-1}e^{-t(\zeta-i)}J_m(t\rho)dt]$, $J_m(^*)$ is the first kind of Bessel function. The stress state at the vicinity of edge can be asymptotically expressed in global z-r coordinates system as [10].

$$\begin{pmatrix}\sigma_{zz}\\ \sigma_{rz}\\ \sigma_{rr}\\ \sigma_{\theta\theta}\end{pmatrix}=\frac{K_I}{\sqrt{2\pi s}}\cos\frac{\phi}{2}\begin{pmatrix}1+\sin\frac{\phi}{2}\sin\frac{3\phi}{2}\\ \sin\frac{\phi}{2}\cos\frac{3\phi}{2}\\ 1-\sin\frac{\phi}{2}\sin\frac{3\phi}{2}\\ 2\nu\end{pmatrix}, \tag{2}$$

where K_I, similar to the crack stress intensity factor, is the contact stress concentration factor, which is related to the external load P as

$$K_I=-\frac{P}{2R\sqrt{\pi R}}, \tag{3}$$

since $P>0$, thus $K_I<0$.

The stresses in Eq. (2) can be also written in the local polar coordinate system in Fig. 1 as:

$$\begin{pmatrix}\sigma_{ss}\\ \sigma_{\phi\phi}\\ \sigma_{s\phi}\\ \sigma_{\theta\theta}\end{pmatrix}=\frac{K_I}{\sqrt{2\pi s}}\begin{pmatrix}\cos\frac{\phi}{2}(1+\sin^2\frac{\phi}{2})\\ \cos^3\frac{\phi}{2}\\ \sin\frac{\phi}{2}\cos^2\frac{\phi}{2}\\ 2\nu\cos\frac{\phi}{2}\end{pmatrix}. \tag{4}$$

It can be seen that the stress distribution Eq. (4) near the contact edge is similar to the stress field of plane strain crack problem. On the basis of the stress distribution, we will analyze the contact cracking mechanism.

2.2. Contact principal stress state

The strength criteria for isotropic materials can be expressed in terms of combination of three principal stresses [27], for examples, the maximum shear stress criterion, Mohr-Coulomb criterion, Huber-Mises criterion. Thus, it is necessary to find the three principal stresses near the contact edge first, which can be computed with the principal stress formulae as

$$\begin{aligned}
\sigma_1 &= \frac{\sigma_{ss}+\sigma_{\phi\phi}}{2}+\sqrt{\sigma_{s\phi}^2+(\frac{\sigma_{ss}-\sigma_{\phi\phi}}{2})^2},\\
\sigma_2 &= \frac{\sigma_{ss}+\sigma_{\phi\phi}}{2}-\sqrt{\sigma_{s\phi}^2+(\frac{\sigma_{ss}-\sigma_{\phi\phi}}{2})^2},\\
\sigma_3 &= \sigma_{\phi\phi}.
\end{aligned} \tag{5}$$

By substituting Eqs. (4) into (5), one obtains

$$\begin{aligned}
\sigma_1 &= \frac{K_I}{\sqrt{2\pi s}}2\nu\cos\frac{\phi}{2}<0,\\
\sigma_2 &= \frac{K_I}{\sqrt{2\pi s}}\cos\frac{\phi}{2}(1-\sin\frac{\phi}{2})<0,\\
\sigma_3 &= \frac{K_I}{\sqrt{2\pi s}}\cos\frac{\phi}{2}(1+\sin\frac{\phi}{2})<0.
\end{aligned} \tag{6}$$

It can be found from Eq. (6) that the three principal stresses approach infinitely large values as $s\to 0$ in Fig. 1. Because $K_I<0$ from Eq. (3), it reveals that the stress state at the vicinity of contact edge is a kind of *very high compressive one*.This stress state completely denies the possibility of employing the maximum tensile stress criterion to predict the contact cracking initiation, which is always employed for brittle materials. More specifically, the three compressive principal stresses at the contact edge similarly rules out the possibility of initiating the Mode I crack. So far, the most remaining possibility is that, at the initial contact damage stage, the shear stress related mechanism triggers the crack initiation with the *high compressive stresses confinement*. This potential mechanism of brittle shear fracturing for rock-like materials will be very different from the common brittle material fracturing by tensile stress, and the other brittle shear fracturing mechanism actually due to multi- tensile-stressed micro-cracks [1], but it needs to be experimentally validated.

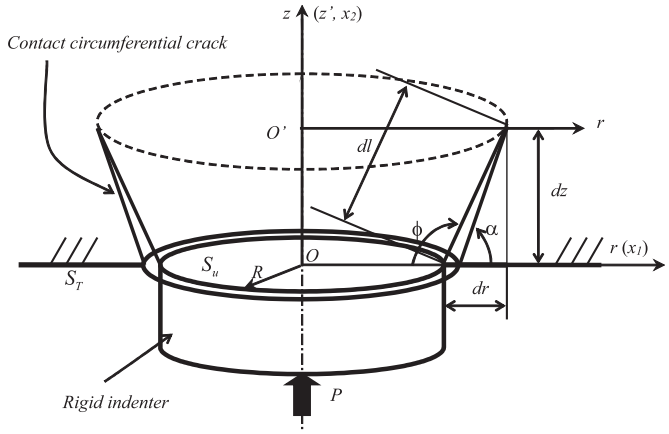

Fig. 3. A schematic of contact crack initiation.The upper elastic solid is indented by a rigid indenter, and a contact ring crack initiates along the contact edge.

3. Contact energy analysis: contact crack initiation energy release rate G

Because the stress is concentrated at the contact edge, it is legitimate to suppose that the crack initiation will start from the edge. Below, we will analyze the crack driving force at the stage of contact crack initiation with the *principle of virtual work*. Consider a 3-D axis-symmetric contact illustrated by Fig. 3 in which the surface S encloses the whole half space. Traction T_i acts on the surface S_T including the contacted surface while the remaining part of the boundary is displacement boundary S_u. Now, consider a circumferential crack tip undergoing a virtual displacement by an infinitesimal distance *dl* orientated at an arbitrary angle ϕ and $dA=2\pi Rdl$ as shown in Fig. 3. Then *the principle of virtual work* for the scenario of contact crack initiation can be written as

$$\delta W=\delta U_E+\delta U_{crack}+\delta U_{diss}, \tag{7}$$

in which, δW is virtual work due to external load, δU_E is the virtual elastic energy stored in the whole solid, δU_{crack} is the virtual energy consumed during forming/closing crack, and δU_{diss} is the dissipation energy mainly due to crack surfaces friction during shear fracturing. They can be expressed, respectively as

$$\begin{aligned}
\delta U_E &= \int_V \delta w dV,\\
\delta W &= \int_S T_j\delta u_j dS,\\
\delta U_{crack} &= G\delta A,\\
\delta U_{diss} &= \tau_0 A\delta l,
\end{aligned} \tag{8}$$

where, V is the volume of the whole half space solid, and the strain energy density w is given by $w=\int_0^{\epsilon_{ij}}\sigma_{ij}d\epsilon_{ij}$; S the whole surface of the body ($S=S_T+S_u$); the parameter G, the crack initiation energy release rate, is also named as crack driving force; τ_0 is the friction stress

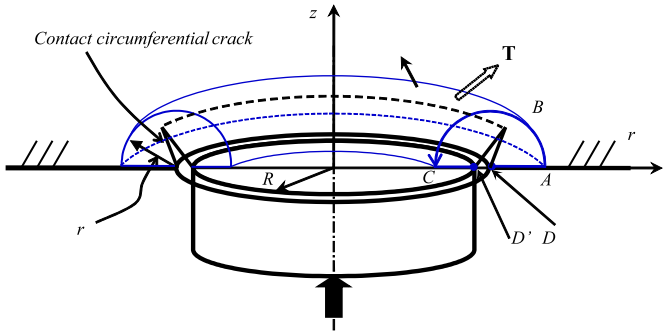

Fig. 4. A schematic of integrals' surface enclosing the contact crack.

between crack surfaces, and A is the area of the formed circumferential crack. Then Eq. (7) can be re-expressed as

$$\begin{aligned}0 &= \delta U_E - \delta W + \delta U_{crack} + \delta U_{diss}\\ &= \int_v \delta w dV - \int_s T_i \delta u_i ds + G\delta A + \tau_0 A\delta l\\ &= \int_v \left(\frac{dw}{dx_j}\frac{dx_j}{dA}\delta A\right)dV - \int_s \left(T_i\frac{du_i}{dx_j}\frac{dx_j}{dA}\delta A\right)ds + G\delta A + \tau_0 A\delta l\\ &= \int_v \left(\frac{dw}{dx_j}\frac{dx_j}{dl}\delta l\right)dV - \int_s \left(T_i\frac{du_i}{dx_j}\frac{dx_j}{dl}\delta l\right)ds + G2\pi R\delta l + \tau_0 2\pi Rl\delta l,\end{aligned} \tag{9}$$

in which, x_1 refers to r and x_2 refers to z in Fig. 3. Since we suppose that the traction boundary condition is fixed, with Eulerian description, the coordinate system can always be chosen so that the origin O lies along the z-axis and in contact surface, even when the contact initiation crack tip is advancing. If we denote $\cos\phi = n_1$, $\sin\phi = n_2$, from Fig. 3, the following relationships can be established

$$\begin{aligned}\frac{dx_1}{dl} &= \frac{dr}{dl} = \cos\alpha = \cos(\pi - \phi) = -\cos\phi = -n_1,\\ \frac{dx_2}{dl} &= \frac{dz}{dl} = -\sin\alpha = -\sin(\pi - \phi) = -\sin\phi = -n_2.\end{aligned} \tag{10}$$

By substituting Eq. (10) into (9),the crack initiation energy release rate in *dl* direction can be written as

$$\begin{aligned}0 &= \int_V w_{,j}(-n_j)\delta l dV - \int_S T_i u_{i,j}(-n_j)\delta l ds + G2\pi R\delta l + \tau_0 2\pi Rl\delta l\\ &= (-n_j\int_V w_{,j}dV + n_j\int_S T_i u_{i,j}ds + 2\pi RG + \tau_0 2\pi Rl)\delta l.\end{aligned} \tag{11}$$

Since δl in Eq. (11) can be an arbitrary value, therefore, we may get the crack driving force as

$$\begin{aligned}G &= \frac{1}{2\pi R}n_j(\int_V w_{,j}dV - \int_S T_i u_{i,j}ds) - \tau_0 l\\ &= \frac{1}{2\pi R}n_j\int_s (wm_i - T_i u_{i,j})ds - \tau_0 l = \frac{1}{2\pi R}n_j J_j - \tau_0 l\end{aligned} \tag{12}$$

or

$$G = \frac{1}{2\pi R}(J_1\cos\phi + J_2\sin\phi) - \tau_0 l = \frac{1}{2\pi R}(J_r\cos\phi + J_z\sin\phi) - \tau_0 l, \tag{13}$$

where $J_j = \int_s (wm_j - T_i u_{i,j})ds$ (j=1,2)are *surface* integrals and m_i is the outward normal unit vector shown in Fig. 4. We can easily prove that they are *surface*-independent integrals just similar to the 2-D *path*-independent integrals introduced by Knowles and Sternberg [28] for crack problems, following the definition of the well-known J-integral (i.e. J_1-integral) by Rice [29]. Originally the concept of such kind of integral was introduced by Eshelby [30].

The crack driving force of contact crack initiation can be obtained by letting $l \to 0$ in Eq. (13) as

$$G = \frac{1}{2\pi R}(J_r\cos\phi + J_z\sin\phi), \tag{14}$$

The intersection line of the integral surface S is the contour s(= $\overline{DABCD'}$) shown on the right hand side in Fig. 4. Since the integrals are surface-independent, we will prove the main result of [31]

$$J_i = \left(\int_S wm_i dS - \int_S T_j\frac{du_j}{dx_i}dS\right) = 2\pi R\lim_{r\to 0}\int_s \left(wm_i - T_j\frac{du_j}{dx_i}\right)ds. \tag{15}$$

By virtue of Eq. (15), we can get

$$\begin{aligned}J_1 = J_r &= 2\pi R\int_s \left(wm_1 - T_j\frac{du_j}{dr}\right)ds = 2\pi R\int_s \left(wm_r - T_j\frac{du_j}{dr}\right)ds\\ &= 2\pi R\frac{(1-\nu^2)}{2E}K_1^2,\\ J_2 = J_z &= 2\pi R\int_s \left(wm_2 - T_j\frac{du_j}{dx_z}\right)ds = 2\pi R\int_s \left(wm_z - T_j\frac{du_j}{dx_z}\right)ds = 0.\end{aligned} \tag{16}$$

By inserting Eq. (16) into (14), we obtain

$$G = \frac{1}{2\pi R}J_r\cos\phi = \frac{(1-\nu^2)}{2E}K_1^2\cos\phi \tag{17}$$

and since $K_I = -\frac{P}{2R\sqrt{\pi R}}$, thus

$$G = \frac{(1-\nu^2)}{2E}K_I^2\cos\phi = \frac{(1-\nu^2)}{8E\pi R^3}P^2\cos\phi. \tag{18}$$

Eq. (18) provides a simple approach to assess the material toughness. No matter whether the maximum shear stress criterion or the Mohr-Coulomb criterion is used, we only need to record the critical external load P_c and measure the initiation angle ϕ. Then submitting them into Eq. (18), the material toughness G_c will be

$$G_c = \frac{(1-\nu^2)}{8E\pi R^3}P^2\cos\phi. \tag{19}$$

Finally, it should be pointed out that, because the crack energy release rate G (or the crack driving force) in Eqs. (18) and (19) must be positive at crack initiation stage, which requires $\cos\phi > 0$. It means that the crack initiation angle ϕ must be less than 90° ($\phi < 90°$).

Thus, in this section, completely from energy point of view, we derived the crack driving force G expression and meanwhile confined the range of contact crack initiation angle. This provides a basic principle which the elastic contact fracture should comply with.

4. Experimental tests

In this section, the experimental tests on typical rock-like materials will be conducted to reveal the rock-like material contact fracturing behavior, and, at the same time, to verify both the undertaken analysis and some theories proposed by others in literature. Because rocks are opaque materials, it is difficult to directly observe a contact crack initiation. In contrast, PMMA (methyl methacrylate) is a brittle non-crystalline material but transparent. It has rock-like mechanical properties at room temperature, and more importantly, its optical transparency enables to directly observe internal deformation. These properties provide a good means to simulate and monitor a damage process. Thus, PMMA has been often used to simulate earthquake, rock fracture and friction in laboratory conditions (e.g. see [32–35]). Thus, we will mainly concentrate on PMMA samples test but the real sandstone test, as a complementary part, will be also studied for further clarification.

4.1. Tests of PMMA

The tests are conducted on the test machine MTS880. The PMMA samples are indented with a relatively rigid cylindrical punch with flat end. The material of indenter employed is YG10X (Tungsten Carbide Rod) whose E=600–630GPa, ν=0.20–0.23. It can be treated as a rigid indenter in comparison with the tested PMMA materials (The material elastic parameters and geometric parameters are listed in Table 1). The experimental setup can be observed in Fig. 5. The load mode is force

Table 1
PMMA specimens and indenter's geometry and elastic properties.

	Geometry	Elastic prpoperties
6 PMMA specimens	$70 \times 70 \times 70\,mm^3$	E=1.8–3.1GPa, $\nu = 0.35 - 0.4$
Indenter (YG10X)	Diameter of indenter end: $D = 20\,mm$, $h = 30\,mm$	E=600–630GPa, $\nu = 0.20 - 0.23$

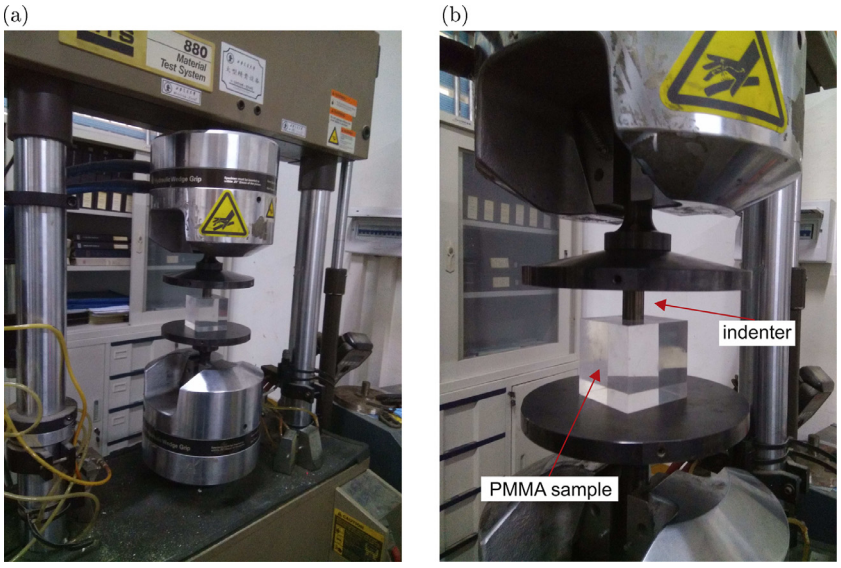

Fig. 5. Photographs of the experimental setup used for PMMA contact damage tests: (a) test rig, (b) indenter and sample.

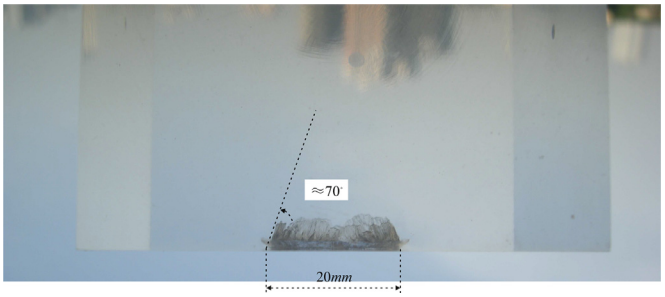

Fig. 6. Side view of crack initiation along contact edge from the indented surface of PMMA.

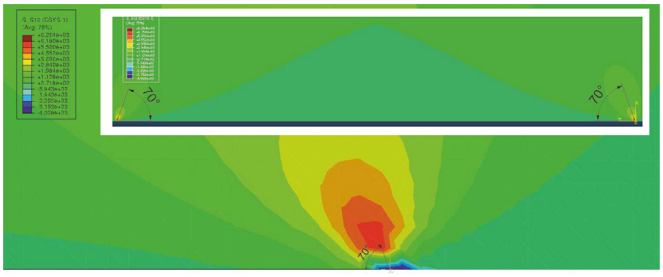

Fig. 7. FE computed local and global shear stress distributions beneath contact edges(The test specimen was meshed with a set of 294,084 2D quadrilateral axisymmetric elements (CAX4R, ABAQUS 6.14) with finer elements (0.03mm) at the contact edge. The interaction between the rigid indenter and the specimen is modelled as a frictionless contact. A 1N load acts from the indenter to the specimen which is supported at its upper base.).

load. Our main aim is to observe the angle of conical crack, critical load, as well as crack growth. Contact crack initiation is observed and photographed. The load against indentation depth is recorded. Six blocks of PMMA respectively indented by relatively rigidly cylindrical punches with flat end are conducted.

Fig. 6 displays the scenario of contact crack initiation where the angle of conical crack is clearly near 70° , which conforms to our energy analysis result ($\phi < 90°$) in Section 3. This promptly raises an intriguing question: which damage criterion is capable of explaining this result? As mentioned before, when the rock-like materials is under such *high compressive stresses confinement* conditions, the shear stress related damage criteria is the first option. To specify the accurate damage criterion for this contact initiation fracturing in Fig. 6, an elastic 2D axisymmetric contact model for the experimental contact prototype is developed utilizing the commercial finite element method package ABAQUS 6.14 to simulate contact stress state. The test specimen is meshed with a set of 294,084 2D quadrilateral axisymmetric elements (CAX4R) with finer elements (0.03 mm) at the contact edge. The elements refinement is performed after a careful mesh sensitivity analysis to ensure convergence of results. The interaction between the rigid indenter (master surface) and the specimen (slave surface) is modelled as a frictionless contact. A 1N load acts from the indenter to the specimen which is supported at its base.

Fig. 7 shows shear stress distribution in local polar coordinate system. It can be observed from both zoomed local edge and the global shear stress inset in Fig. 7 that the maximum shear stress underneath the contact edge is about 70°. This is in a very good agreement with our experimental result, which evidently suggests that the maximum shear stress is more suitable for contact fracturing in this study.

Although the volume of PMMA blocks is finite, the stress state at the vicinity of contact edge can be approximated with the expression of Eq. (4), because, compared with the contact edge zone, block can be treated as an infinite body. Thus, reversely, by using the maximum shear stress criterion, the crack initiation angle for contact can be analytically calculated from Eq. (4) as

$$\frac{\partial \theta_{s\phi}}{\partial \phi} = \frac{K_I}{\sqrt{2\pi s}}\left(\frac{1}{2}\cos^2\frac{\phi}{2} - \sin^2\frac{\phi}{2}\right)\cos\frac{\phi}{2} = 0, \tag{20}$$

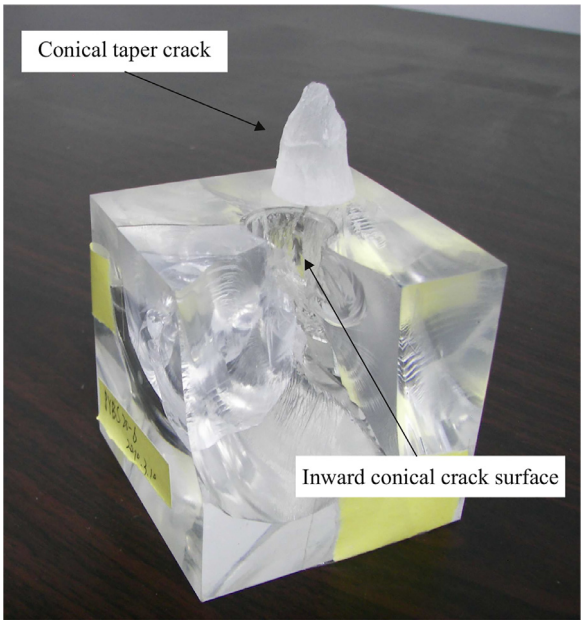

Fig. 8. Inward conical crack of PMMA after finial catastrophic contact fracture.

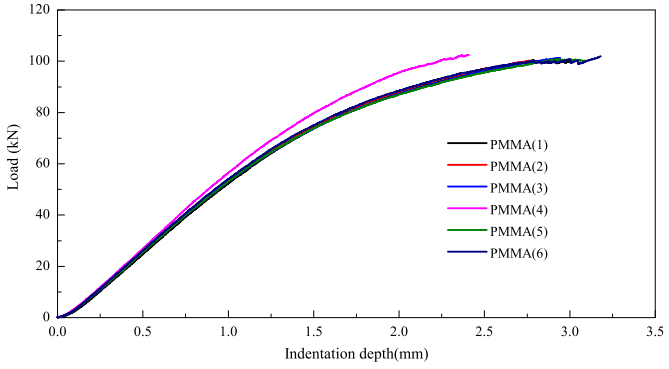

Fig. 9. Load versus indentation depth curves. The critical load is reached at finial catastrophic contact fracture.

whose solution is

$$\cos\phi = \frac{1}{3}, \phi = 70.5288°. \tag{21}$$

So far, it can be concluded that both experimental results and numerical simulation indicate that the maximum shear stress triggered contact brittle shear fracturing.

The finial catastrophic fracture scenario is shown by Fig. 8, which also reveals that the shear stress triggered contact brittle shear fracturing. More importantly, Fig. 8 shows that the crack can also grow along the initiation angle under this condition. This test is very repeatable, which can be found from Fig. 9, in which the relation between load and indentation depth is plotted. Unfortunately, it is hard to identify the critical load value P_c for Eq. (19)

4.2. Test of sandstone

Sandstone is another brittle material and thus seven sandstone specimens are tested with a Tungsten Carbide rod in a similar way as conducted on PMMA utilizing Instron test machine. As previously mentioned, the indenter can be treated as a rigid body compared to sandstone.The indenter and sandstone specimens' geometry parameters are given in Table 2. Since this rock is opaque, it is difficult to obtain a direct information on contact crack initiation but the uniformly finial

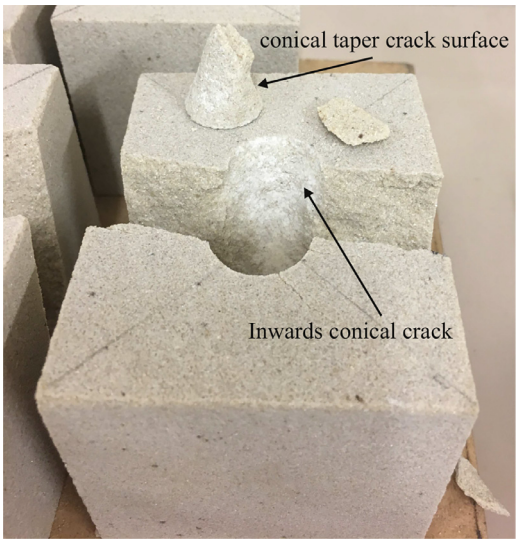

Fig. 10. Top view of contact fracture of sandstone showing a conical taper crack.

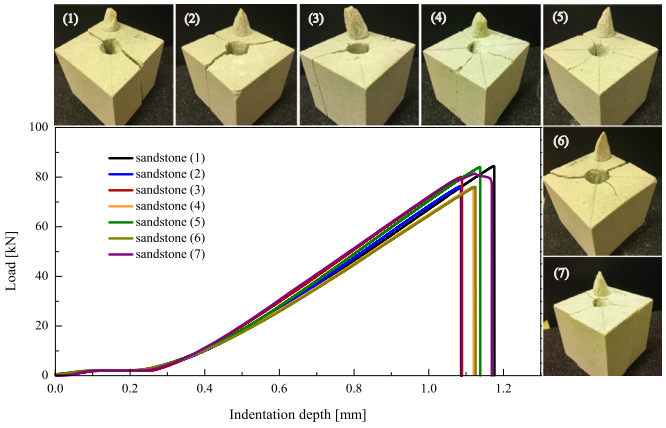

Fig. 11. Experimental results showing load versus indentation depth relationships for conical contact fractures of sandstone specimens. The critical loads are reached at finial catastrophic contact fracture. The repeatability is demonstrated by photographs of seven tests.

catastrophic contact fracture scenario may reveal some contact fracturing information (See Fig. 10).

Fig. 10 depicts one of the uniformly contact broken scenarios of sandstone specimens. It can be observed that the angle of conical taper crack is also near 70°. Again, these results imply that the maximum shear stress criterion is more suitable for sandstone contact damage, and the crack growth is also dominant by shear stress. This suggests the same conclusion as we did in PMMA test. Fig. 11 shows the load versus indentation depth which is recorded for all sandstone samples until fracture. As represented in the graph, there is a close match between the critical damage loads and displacements of sandstone samples. This is possibly because sandstone material is considered to be an approximately homogenous rock.

The force loading rate for the main experiments on sandstone specimen was kept at the lowest possible rate (0.05 mm/min) in order to decrease the dynamic effect. The effect of loading rate on sandstone contact fracturing and its critical loads and indentation depths are represented in Fig. 12. It can be found that the critical damage load and displacement are slightly increased at higher loading velocities but they are in the range of acceptable data dispersion of Fig. 11. In experiments with higher loading velocities, it was detected that the shape and angle of conical crack are not exactly the same as the ones with 0.05 mm/min

Table 2
Sandstone specimens and indenters' geometry parameters.

	Geometry	Elastic prpoperties
7 Sandstone specimens	$70 \times 70 \times 70\,mm^3$	E=27−29–GPa, $\nu = 0.07 - 0.12$
Indenter (YG10X)	Diameter of indenter end: $D = 20mm$, $h = 30mm$	E=600−630GPa, $\nu = 0.20 - 0.23$

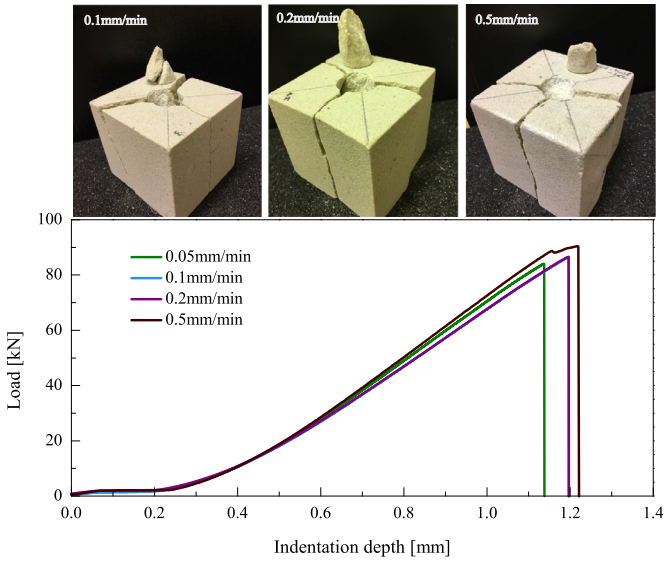

Fig. 12. Experimental results showing load versus indentation depth relationships for conical contact fractures of sandstone specimens with different loading rates. The critical loads are reached at finial catastrophic contact fracture.

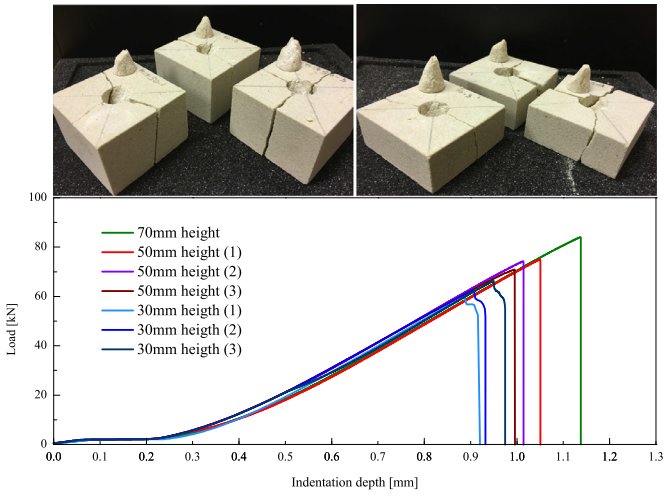

Fig. 13. Experimental results showing load versus indentation depth relationships for conical contact fractures of sandstone specimens with different sample heights. The critical loads are reached at finial catastrophic contact fracture. The repeatability is demonstrated by photographs of three tests for each sample height.

which shows that contact crack growth at higher loading rates may not be fully dominated by shear stress.

Specimen dimension is also an effective parameter on sandstone contact fracturing behaviour. Various sandstone samples with different heights were tested while all other test parameters were kept the same and the results are shown in Fig. 13. As represented, samples with smaller heights are damaged at lower load and indentation depth values. As shown in the figure, the inward conical taper cracks for these experiments have angle of around 70°.

Water content is one of the crucial factors affecting rock strength. In order to study how this factor influences sandstone contact damage behaviour, some samples were saturated to 7% water content with water utilizing a vacuum device and tested while all other experimental conditions were kept the same. Fig. 14 demonstrates a significant decrease of critical damage load and displacement values for saturated samples compared to dry one. It was observed that the conical taper crack is also around 70° for wet sandstone.

4.3. Discussion

PMMA tests display a visible contact brittle shear fracturing. The crack initiation angle is clearly near 70°. The experimental results demonstrate that its fracturing behavior is in line with the maximum shear stress criterion in the case of high compressive stress confinement condition. The additional sand stone tests also show similar result. This finding is evidently different from the result reported by Healy et al. [1], where they modeled brittle shear fracturing with tensile micro-cracks interaction mechanism. However, why is the contact fracture pattern of glass (see Fig. 2) different from PMMA and sandstone's? A couple of possible factors may be associated with this phenomenon: *(i) Multi-micro-crack mechanism* [1,14,36]. When the brittle glass materials with multi-micro-crack under compression, the micro-cracks in-

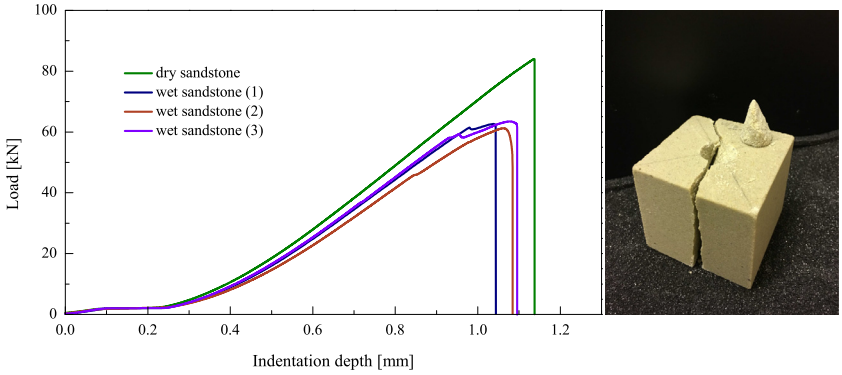

Fig. 14. Experimental results showing load versus indentation depth relationships for conical contact fractures of three water-saturated sandstone specimens. The critical loads are reached at finial catastrophic contact fracture.

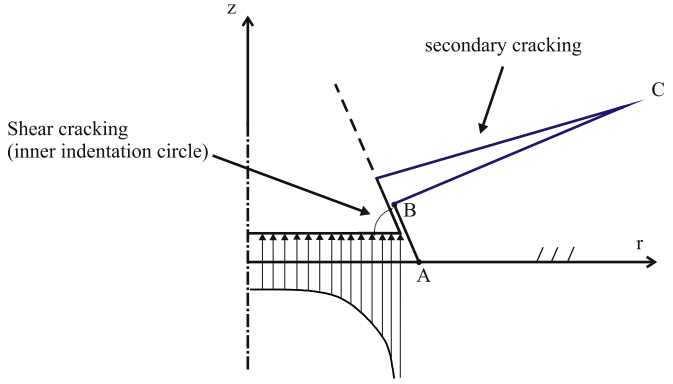

Fig. 15. Contact secondary cracking mechanism for brittle glass. Cracking in sequence: (1). Shear stress leads shear fracturing AB at the perfect contact edge under compressive stress state; (2). the shear cracking changes global stress state, and the positive circumferential tensile stress at the crack-tip B triggers the secondary opening conical crack BC.

teraction may result tensile stress on micro-cracks, which can trigger micro-cracks growth and coalition, and finally lead this result. *(ii) Secondary cracking* [37], which can be explained with help of Fig. 15. At the initial stage, the contact crack in glass is very short and the crack obeys the maximum shear stress criterion, but once the crack grows and simultaneously stress state is changed, the maximum tensile stress criterion is prevailing. So far, we would be in favor of the second explanation, but, clearly, a careful and thorough study on contact fracturing of glass is still needed to be conducted. This study will be addressed elsewhere.

5. Conclusions

Contact conical crack initiation of rock-like brittle materials indented by rigid cylindrical punches with flat end has been studied. Two main conclusions can be drawn as follows:

(i) A new phenomenon of shear stress triggered shear fracturing in rock-like brittle materials has been found, which is evidently distinct from the traditional shear fracturing mechanism due to multi- tensile-stressed micro-cracks in materials [1].

(ii) The contact crack initiation angle for such kind rock-like materials, different from the reports in literatures such as Hertzian crack and Roesler [2], has been observed inwards rather than outwards. This finding testifies that the rock-like brittle material shear fracturing along its maximum shear stress plane is possible under some special confinement. The mechanism of such results has been discussed with basic stress analysis and the energy principle.

The rock-like material represents a broad spectrum of materials which have various applications. This study is a new understanding of the mechanical behavior of rock-like materials. Especially, it has important implications for seismology and rock-mass stability, as well as rock engineering such as rock drilling.

Acknowledgments

L. Ma would like to thank the partial support by National Natural Science Foundation of China (Grant No.: 41630634).

References

[1] Healy D, Jones RR, Holdsworth RE. Three-dimensional brittle shear fracturing by tensile crack interaction. Nature 2006;439:64–7.
[2] Roesler F. Brittle fractures near equilibrium. Proc Phys Soc 1956;69:981–92.
[3] Lawn BR. Indentation of ceramics with spheres: a century after hertz. J Am Ceram Soc 1998;81:1994–8.
[4] Frank F.C., Lawn B.R. On the theory of hertzian fracture. Proceeding of the royal society of london A2991967;:291–306.
[5] Wilshaw TR. The hertzian fracture test. J Phys D Appl Phys 1971;4:1567–81.
[6] Lawn BR, Wilshaw TR. Indentation fracture: principles and applications. J Mater Sci 1975;10:1049–81.
[7] Warren PD. Determining the fracture toughness of brittle materials by hertzian indentation. J Eur Ceram Soc 1995;15:201–7.
[8] Geandier G, Denis S, Mocellin A. Float glass fracture toughness determination by hertzian contact: experiments and analysis. J Non Cryst Sol 2003;318:284–295.
[9] Mouginot R, Maugis D. Fracture indentation beneath flat and spherical punches. J Mater Sci 1985;20:4354–76.
[10] Giannakopoulos AE, Lindley TC, Suresh S. Aspects of equivalence between contact mechanics and fracture mechanics: theoretical connections and life-prediction methodology for fretting-fatigue. Acta Mater 1998;46:2855–968.
[11] Bieniawski ZT. Mechanism of brittle fracture of rock: part I theory of the fracture process. Int J Rock Mech Min Sci 1967;4:395–406.
[12] Bieniawski ZT. Mechanism of brittle fracture of rock: part II-experimental studies. Int J Rock Mech Min Sci 1967;4:407–23.
[13] Steif PS. Crack extension under compressive loading. Eng Fract Mech 1984;20:463–73.
[14] Ashby MF, Hallam SD. The failure of brittle solids containing small cracks under compressive stress states. Acta Metall 1986;34:497–510.
[15] Horri H, Nemat-Nasser S. Brittle failure in compression: splitting, faulting and brittle-ductile transition. Philos Trans Royal Soc A319 1986:337–74.
[16] Ashby MF, Sammis CG. The damage mechanics of brittle solids in compression. Pure Appl Geophys 1990;133:489–521.
[17] Paterson MS, Wong TF. Experimental rock deformation-the brittle field. New York: Springer Science and Business Media; 2005.
[18] Hoek E, Martin CD. Fracture initiation and propagation in intact rock - a review. J Rock Mech Geotech Eng 2014;6:287–300.
[19] Cheng H, Zhou J, Zhou QQ. The effects of crack openings on crack initiation, propagation and coalescence behavior in rock-Like materials under uniaxial compression. Rock Mech Rock Eng 2016;49:3481–94.
[20] Tang SB, Bao CY, Liu HY. Brittle fracture of rock under combined tensile and compressive loading conditions. Canad Geotech J 2017;54:88–101.
[21] Kocer C, Collins RE. Angle of hertzian cracks. J Am Ceram Soci 1998;81:1736–1742.
[22] Xie YJ, Hu XZ, Chen J, Lee KY. Micro-indentation fracture from flat-ended cylindrical indenter. Fatigue Fract Eng Mater Struct 2011;35:45–55.
[23] Xie YJ, Hills D, Hu XZ. Cone crack initiation induced by contact from cylindrical punch. J Mater Sci 2007;42:9469–75.
[24] Ma L, Korsunsky AM. On the use of vector J-integral in crack growth criterion for brittle solids. Int J Fract 2005;133:L39–46.
[25] Petit JP, Barquins M. Can natural faults propagate under mode II conditions? Tectonics 1988;7:1243–56.
[26] Sneddon IN. Boussinesq'S problem for a flat-ended cylinder. Math Proc Camb Philos Soc 1946;42:29–39.
[27] Yu MH. Unified strength theory and its applications. Springer; 2004.
[28] Knowles JK, Sternberg E. On a class of conservation laws in linearized and finite elastostatics. Arch Ration Mech Anal 1972;44:187–211.
[29] Rice JR. A path independent integral and the approximate analysis of strain concentration by notches and cracks. J Appl Mech 1968;35:379–86.
[30] Eshelby JD. The force on an elastic singularity. Philos Transe Royal Soc Lond 1951;A244:87–112.
[31] Budiansky B, O' Connell RJ. Elastic moduli of a cracked solid. Int J Solids Struct 1976;12:81–97.
[32] Rubinstein SM, Cohen G, Fineberg J. Detachment fronts and the onset of dynamic friction. Nature 2004;34:1005–9.
[33] Lengline O, Elkhoury JE, Daniel G, Schmittbuhl J, Toussaint R, Ampuero JP, et al. Interplay of seismic and aseismic deformations during earthquake swarms: an experimental approach. Earth Planet Sci Lett 2012;331–332:215–23.
[34] Langer S, Weatherley D, Olsen-Kettle L, Finzi Y. Stress heterogeneities in earthquake rupture experiments with material contrasts. J Mech Phys Sol 2013;61:742–61.
[35] Svetlizky I, Fineberg J. Classical shear cracks drive the onset of dry frictional motion. Nature 2014;509:205–8.
[36] Paliwal B, Ramesh KT. An interacting micro-crack damage model for failure of brittle materials under compression. J Mech Phys Sol 2008;56:896–923.
[37] Renshaw CF, Schulson EM. Universal behaviour in compressive failure of brittle materials. Nature 2001;412:897–900.